



Effective removal of arsenic from an aqueous solution by ferrihydrite/goethite graphene oxide composites using the modified Hummers method

M. Vazquez-Jaime^a, J.A. Arcibar-Orozco^b, C.E. Damian-Ascencio^c, A.L. Saldaña-Robles^d, M. Martínez-Rosales^e, A. Saldaña-Robles^{d,*}, S. Cano-Andrade^c

^a Graduate Program in Biosciences, Universidad de Guanajuato, Irapuato, GTO 36500, Mexico

^b CIATEC A.C. Centro de Innovación Aplicada en Tecnología Competitiva, Omega 201, Industrial Delta, León, GTO 37545, Mexico

^c Department of Mechanical Engineering, Universidad de Guanajuato, Salamanca, GTO 36885, Mexico

^d Department of Agricultural Mechanical Engineering, Universidad de Guanajuato, Irapuato, GTO 36500, Mexico

^e Department of Chemical Engineering, Universidad de Guanajuato, Guanajuato, GTO 36050, Mexico

ARTICLE INFO

Keywords:

Graphene oxide
Goethite
Ferrihydrite
Arsenic removal
Modified Hummers method

ABSTRACT

This work presents the synthesis of graphene oxide and modified graphene oxide by adding oxygenated groups, using the modified Hummers method. The synthesized materials are characterized by Fourier-transform infrared spectroscopy, X-ray, isotherm adsorption curves, and kinetic adsorption tests. In addition, two varieties of ferric hydroxides, i.e., goethite and ferrihydrite, are coupled to the graphene oxide and the modified graphene oxide, and their arsenic adsorption properties are studied. Results show that the modified composites have a deviation from the linear van't Hoff equation, suggesting that multiple interactions and a multi-layer adsorption are occurring. Also, the results show that composites of graphene oxide/or modified graphene oxide with goethite have a better adsorption capacity than those coupled to ferrihydrite.

1. Introduction

The contamination of groundwater is a problem that affects several countries around the world. In particular, the presence arsenic (As) in water mantles, which is caused by anthropogenic and natural conditions, makes the contamination by this heavy metal a serious problem in a large number of countries because of its high toxicity and carcinogenic properties. For instance, in Latin America, at least 14 countries have problems with As in groundwater [1,2]. The main forms of inorganic arsenic that are present in groundwater in natural forms are its oxidation states +3 and +5. These oxidation forms are commonly found as trivalent arsenite and pentavalent arsenate, which are dangerous for human health and the environment [3,4]. Thus, as a measure to mitigate this problem, several organizations such as the World Health Organization (WHO) have established a maximum concentration of As in water of 0.01 mg L^{-1} .

To tackle this problem, several technologies for the remotion of As (V) and As(III) have been developed. Such technologies include physicochemical processes such as coagulation and oxidation followed by coagulation [5–7], precipitation [8], separation membranes [9],

biological remediation [10], adsorption [4,11], among others. Specifically, adsorption is one of the most used methods to remove arsenic and is considered an economic and efficient solution [12]. Also, a wide variety of adsorbent materials have been used to remove arsenic, such as those based on 3-(2-aminoethylamino)propyltrimethoxysilane (AAPTS) [13,14], 3-[2-(2-aminoethylamino)ethylamino]propyl-trimethoxysilane (AAPTS) [15], ferric oxides, metallic oxides, activated carbon, zeolites, agroindustrial remnants, among others [16–26].

Graphene has been employed in several applications of arsenic adsorption. In particular, the graphene oxide (GO) is of interest as an adsorbent material because of its laminar structure, surface area, and ease of synthesis. Also, the GO contains several oxygenated groups such as hydroxyl, epoxy, carbonyl, and carboxylic acids [27,28]. In addition, it has been shown that the modification of the surface material has a positive impact on the arsenic removal because the presence of functional groups helps to increase the adsorption on the surface of the GO [29]. For instance, the adsorption properties of As on GO can be improved by doping it with Fe [1]. Thus, it is expected that the oxidation grade of the GO and the kind of functional groups added to it have a

* Corresponding author.

E-mail address: adriana.saldana@ugto.mx (A. Saldaña-Robles).

positive impact in the surface properties and the adsorption process [27–32]. Since the oxidation grade and the functional groups are key factors in the adsorption properties of the GO, it is important to understand well their effect on the adsorption of As, especially on the adsorption of As(V) which is the oxidation state more abundant in groundwater.

This work presents the synthesis of GO and MGO by adding oxygenated groups. The materials are synthesized using the modified Hummers method because it assures that adding NaNO₃ allows to obtain up to 63% of oxygenated groups in the materials. The synthesized GO and MGO are also coupled to goethite and ferrihydrite. A characterization of the materials is developed and their adsorptive capacities are also obtained. These materials can be used in water filters to absorb the As(V) naturally present in groundwater so that it can be safely used for drinking or crop irrigation.

2. Experiments

2.1. Materials and methods

The synthesis of GO is prepared by using graphite powder (<20 µm, Sigma Aldrich), sulfuric acid, potassium permanganate, hydrogen peroxide, sodium nitrate, and hydrochloric acid. All of the chemicals are reagent grade (Merck) with no further purification. Arsenate solutions are prepared by dissolving Na₂H·AsO₄·7H₂O (Sigma Aldrich) in water. Deionized water is used for all solutions.

2.2. Synthesis of the GO

2.2.1. Hummers method

The GO is synthesized according to the method given in Ref. [33]. Graphite powder (1.0 g) is added to 23 mL of concentrated sulfuric acid and is stirred at 0 °C. Then, 3.0 g of KMnO₄ are added gradually. The solution is placed in an ice bath to keep the temperature below 20 °C. Subsequently, the solution is stirred for 30 min and 23.0 mL of water are added slowly. Then, the mixture is stirred for 30 min and diluted to 135 mL. After that, 10 mL of hydrogen peroxide (30%) are added. The suspension is left overnight and the resulting graphite oxide is washed using water until a pH of 3 is obtained and no remaining of SO₄²⁻ is detected. The solids are dried at –20 °C [34]. Finally, the graphite oxide is subject to ultrasound irradiation for 2 h to obtain the GO.

2.2.2. Hummers method modified with NaNO₃

The Hummers method employed is modified by adding NaNO₃ as an oxidant agent. The methodology used to synthesize the MGO is that given in [35]. Initially, 1 g of graphite powder and 0.5 g of NaNO₃ are added to 23 mL of concentrated sulfuric acid. Then, 3 g of KMnO₄ are added gradually. The solution is placed in an ice bath to keep the temperature below 20 °C. Subsequently, the solution is stirred for 2 h and 46 mL of water are added slowly. Then, the mixture is diluted with 140 mL of water and 10 mL of hydrogen peroxide (30%). The resulting graphite oxide is washed five times with HCl (5%) and is dried in an oven at 70 °C for 12 h. Finally, the graphite oxide is subject to ultrasound irradiation for 2 h to obtain the MGO.

2.3. Composites Fe-O_x/graphene oxide

Ferrihydrite-GO/MGO and Goethite-GO/MGO composites are synthesized by using the co-precipitation method as follows:

a) The graphene oxide suspension (1 g of GO/MGO in 100 mL of water) is diluted with 830 mL of FeCl₃·6H₂O (0.1 M) under stirring. Then 215 mL of NaOH (0.01 M) are added at a rate of 5 mL min⁻¹. After that, the precipitate is filtered using a Buchner funnel. Finally, the

precipitate is washed and dried in an oven at 35 °C for 24 h. The final product is 7.66 mg of FeO_x-GO-90 and FeO_x-MGO-90.

b) The graphene oxide suspension (1 g of GO/MGO in 100 mL of water) is diluted with 970 mL of Fe(NO₃)₃·9H₂O (0.1 M) under stirring. Then 200 mL of KOH (0.1 M) are added at a rate of 5 mL min⁻¹. After that, the precipitate is filtered using a Buchner funnel. Finally, the precipitate is washed and dried in an oven at 70 °C for 60 h. The final product is 7.57 g of α-Fe³⁺O(OH)-GO-90 and α-Fe³⁺O(OH)-MGO-90.

2.4. Characterization of the MGO

The fast arsenic adsorption test is developed at 25 °C and a pH of 4. The best nanocomposite is selected for characterization and adsorption tests are developed at three different temperatures and three different pH.

2.4.1. Arsenic adsorption experiment

The arsenic adsorption tests are carried out at three different temperatures, i.e., 25 °C, 35 °C, and 45 °C, for each of the three different pH, i.e., 4, 6, and 8. The batch equilibrium adsorption tests are developed at 11 different initial concentrations of As(V), i.e., 0, 1, 2, 3, 4, 5, 6, 7, 8, 9, and 10 mg L⁻¹. Adsorption isotherms are obtained by adding 4 mg of FeO_x-GO-90, FeO_x-MGO-90, α-Fe³⁺O(OH)-GO-90, and α-Fe³⁺O(OH)-MGO-90 to 50 mL of each of the eleven arsenic solutions. The flasks are stirred at 160 rpm using an IKA KS 3000 I control for 72 h until equilibrium is reached. The pH of each sample is adjusted using a solution of either HNO₃ or NaOH. Finally, the samples are filtered (precautions are taken to ensure that the filter paper does not interfere with the arsenic adsorption) and the concentrations are determined with a UV-Vis spectrometer (PerkinElmer LAMBDA 365) by using the molybdenum blue method [36].

The methodology for the determination of As is as follows. 5.2 g of ammonium molybdate and 8.8 mg of potassium antimonyl tartrate in 30 mL are dispersed in 9 mol L⁻¹ sulfuric acid and diluted with deionized water to a final volume of 50 mL in a volumetric flask. This solution is stored in an amber container. Then, 0.0126 g of KMnO₄ are dissolved in 100 mL of distilled water and stirred. This KMnO₄ solution is also stored in an amber flask. Also, an ascorbic acid solution is prepared by adding 1.08 g of ascorbic acid in 10 mL of distilled water. For the preparation of the As sample, 8.8 mL of the sample are used and 0.1 mL of the KMnO₄ solution are poured in a 10 mL volumetric flask. The dilution is stirred for 45 s to assure a uniform mixture of the constituents. Immediately after that, 0.1 mL of 98% H₂SO₄ are added and the solution is shaken again for 45 s. Then, 0.4 mL of the molybdate reagent solution is added and the solution is shaken again for 45 s. After that, 0.2 mL of the ascorbic acid solution is added and the solution is shaken again. Finally, distilled water is added until 10 mL are reached. The final mixture is heated in an oven at 40 °C for 20 min and the absorbance is measured at 845 nm (UV-Vis).

The analyte concentration is obtained as

$$C_{\text{sample}} = \frac{V_{\text{total}} C_{\text{measure}}}{V_{\text{sample}}} \quad (1)$$

where C_{sample} is the As concentration of the sample and V_{measure} is the measure of the As concentration by the UV-Vis spectrophotometer.

2.4.2. X-ray diffraction (XRD)

The XRD results are obtained in a Philips X'pert spectrometer with Cu Kα radiation, at angles (2θ) between 10° and 90°, and a step of 0.06° at 40 kV and 30 mA.

2.4.3. FTIR spectroscopy

The FTIR analyses are carried out in a Thermo Scientific NICOLET IS10 at attenuated total reflectance (ATR). The spectrum is generated at 128 scans, 4 cm⁻¹ of resolution, and wave numbers between 4000 and

400 cm⁻¹.

2.4.4. Specific surface area and porosity

The specific surface area and porosity of the materials are measured using a Micromeritics TriStar II Plus 2.03 equipment by N₂ adsorption at -196 °C before the sample is degassed at 60 °C to a vacuum of 10⁻⁴ atm for 2 h. The Brunauer-Emmet-Teller (BET) and Barret-Joiner-Halenda (BJH) relations are used to calculate the specific surface area and pore volume, respectively.

2.4.5. Determination of the surface charge distribution

The surface charge distribution is obtained by adding 100 mg of the material to 50 mL of a NaCl 0.1 M electrolyte solution. After 2 h of contact, the suspension is bubbled with N₂ in order to avoid interferences for CO₂ dissolution. After that, the suspension is slightly acidified by adding 0.1 M HCl. Finally, the suspension is titrated with NaOH in a 916 Ti-touch (Metrohom). The surface charge distribution is obtained by determining the proton binding curve, such as

$$Q = \frac{1}{m} [V_0(H_s - OH_s) + V_t N_t - (V_0 + V_t)(H_f - OH_f)] \quad (2)$$

where Q is the amount of adsorbed or released protons from the surface, V_0 and V_t are the solution and titrant added volumes, N_t is the normality of titrant, m is the titrated mass and the suffixes s and f stand for the starting and final concentrations of H⁺ and OH⁻ ions by using the Davies equation [16]. The pH at the point of zero charge (pHPZC) is defined as the intercept of the charge with the x -axis and corresponds to the point in which the net surface charge due to proton adsorption is zero.

2.4.6. XPS analysis

The MGOGH is analyzed by X-Ray Photoelectron Spectroscopy (XPS) using a Thermo Scientific spectrometer with a k-alpha X-ray like excitation source (1486.6 eV), between 292 eV and 288 eV. The binding energies are referenced to the C1s peak at 284.6 eV and fitted with the XPSpeak41 program with a Shirley background subtraction and a Gaussian-Lorentzian as a fitting function. The spectra data is deconvoluted. X-ray photoelectron spectroscopy (XPS) measurements are conducted using a X-ray photoelectron spectrometer (ESCALAB 250Xi, Thermo Fisher, USA). The X-ray radiation source is monochromatic Al K (1486.74 eV) and the photoexcited electrons are analyzed in constant pass energy mode with a pass energy of 50 eV. For comparison, all spectra are referenced to 284.5 eV, corresponding to the C1s region. The XPSPEAK41 software is used for data processing. Core level curve fitting of the different components is performed using a Shirley background.

2.4.7. Raman analysis

The MGOGH is analyzed by RAMAN spectra with a RENISHAW (InVia) Raman Microscopy with a laser frequency of 514 nm as an excitation source. The laser spot size is 1 μm and the power at the sample is kept below 10 mW, in order to avoid laser induced heating. The Raman spectra are recorded with a RENISHAW (M005-141) Raman system with a laser frequency of 514 nm as an excitation source. The laser spot size is 1 μm and the power at the sample is kept below 10 mW, in order to avoid laser induced heating. The ultrasound irradiation for the exfoliation of the graphitic oxide into monolayers of GO is carried out on a SONIC VCX 750 model (20 kHz, 750 W) using a direct immersion titanium horn.

2.4.8. Adsorption isotherms

The Freundlich model is commonly used to estimate the maximum adsorption capacity of As(V). The Freundlich isotherm is given as

$$q_e = K_F C_e^{1/n} \quad (3)$$

where q_e (mg g⁻¹) is the amount of As(V) adsorbed at pseudo-equilibrium, K_F is a measure of the adsorption capacity at a specific

solution phase concentration, C_e (mg L⁻¹) is the pseudo-equilibrium concentration, and $1/n$ is considered a measure of the surface heterogeneity and surface affinity of the solute.

The Langmuir model implies that the adsorption occurs at one superficial layer and that the adsorption rate balances the desorption rate, which is assumed as a constant energy adsorption. This implies a uniform surface. The Langmuir isotherm is given as

$$q_e = \frac{q_L b C_e}{1 + b C_e} \quad (4)$$

where q_e is the adsorption capacity, C_e is the adsorbate concentration at equilibrium, q_L is the maximum adsorption, and b is the Langmuir constant related to the change of Gibbs free energy, ΔG^0 , given as

$$\ln K_d = -\frac{\Delta G^0}{RT} \quad (5)$$

where R is the universal gas constant and T is the absolute temperature. The adsorption constant is determined either from the isotherm, $K_d = b$, hence K_d is numerically equal to b and dimensionless. This observation is in agreement with previous works [37]. The magnitude of the Gibbs free energy is associated with a specific interaction, i.e., a ΔG^0 of about 4 kJ/mol is related to a hydrophobic force, and that of about 4–10 kJ/mol is related with Van der Waals forces. Eq. (5) is modified by including a non-linear dependence on $1/T$ to account for a multiple retention mechanism and interactions. The non-linear behavior occurs when one of the species is distributed between the mobile phase and the stationary phase. Thus, more than one type of interactions take place. The equilibrium constant for the overall process is given as

$$K = \frac{\sum_{S_i} [A_1]_{S_i}}{\sum_{m_i} [A_1]_{m_i}} \quad (6)$$

and, thus, Eq. (5) takes the form

$$\ln K_d = a + \frac{b}{T} + \frac{c}{T^2} \quad (7)$$

where $-\Delta H = R(b + 2c/T)$ and $\Delta S = R(a - c/T^2)$, and the constants a , b , and c are found by numerical regression.

3. Results and discussion

The adsorbent properties of the MGO coupled to ferrihydrite (MGOFH) and goethite (MGOGH) are compared to those of the GO coupled to ferrihydrite (GOFH) and goethite (GOGH), in order to study its advantages as an adsorbent.

3.1. SEM analysis

Fig. 1 shows the SEM images for the goethite (GH), MGO, MGOFH, and MGOGH. It is observed that the goethite presents a crystalline structure, which is usual for this type of material. It is also observed a crystalline structure for the MGO. It is also observed that the grow of ferrihydrite and goethite on the MGO is in an amorphous manner, suggesting that the crystalline structure is lost once a composite with MGO is formed.

3.2. FTIR for the base materials

The FTIR is employed to characterize the oxygen functional groups because the adsorption capacity in the surface of the materials depends on the chemical reactivity of these groups. Thus, the presence of these groups improves the arsenic adsorption.

Fig. 2 shows the FTIR for the GO, MGO, and the synthesized ferrihydrite. The spectra shows bands located at 680 cm⁻¹ and 1040 cm⁻¹ which correspond to an epoxi-stretch (C=O=C) located over the basal

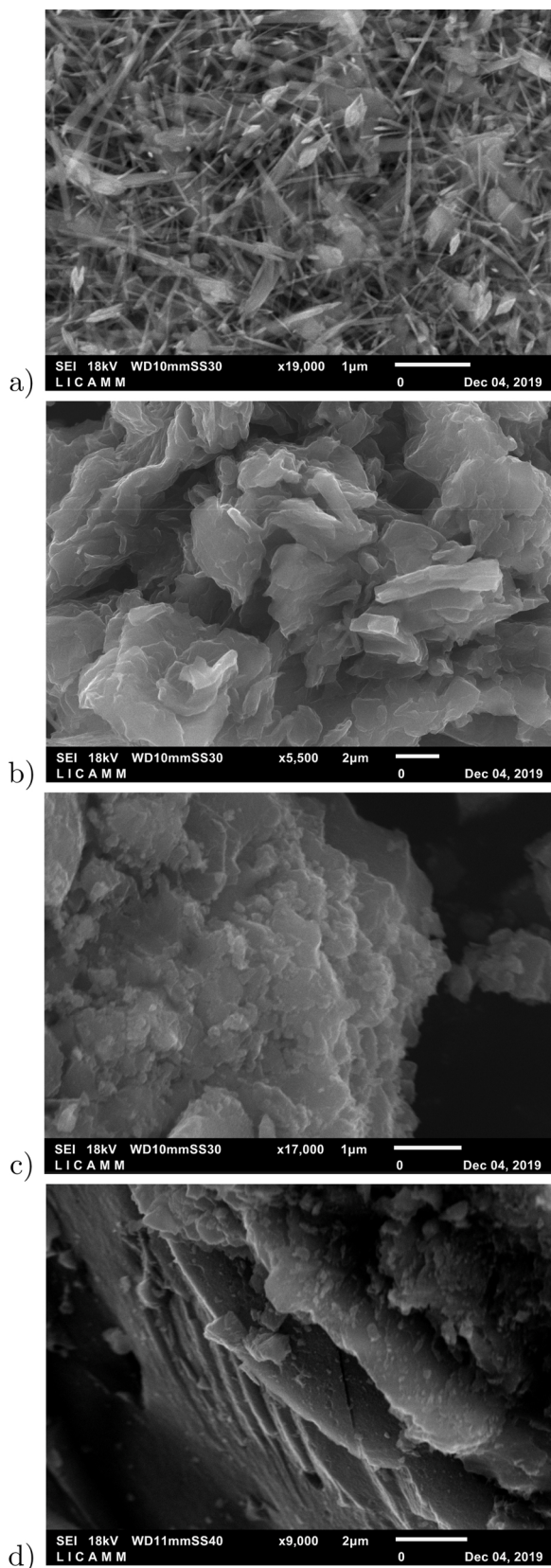


Fig. 1. SEM images for the (a) goethite, (b) modified graphene oxide, (c) modified graphene oxide coupled to ferrihydrite, and (d) modified graphene oxide coupled to goethite.

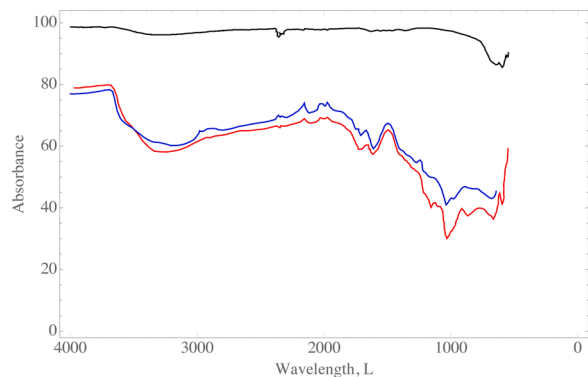


Fig. 2. FTIR for the graphene oxide (blue line), the modified graphene oxide (red line), and the synthesized ferrihydrite (black line).

plane of the GO [35]. The peaks located between 1220 cm^{-1} and 1370 cm^{-1} are related to a flexion mode of hydroxil groups ($\text{C}=\text{O}$). The peaks located at 1600 cm^{-1} and 1650 cm^{-1} are related to a double conjugated bond ($\text{C}=\text{C}$). The bands located between 1720 cm^{-1} and 1750 cm^{-1} correspond to carbonyl functional groups (COOH and $\text{C}=\text{O}$). The $\text{O}-\text{H}$ bands located at 3000 cm^{-1} and 3500 cm^{-1} are due to the humidity of the sample. It is important to realize that even when the oxygen-carbon relation does not vary considerably for the GO and MGO materials, it is possible to identify well defined bands between them and, thus, it is possible to conclude that the molecular structure of each graphene oxide depends considerably on the synthesis conditions.

The FTIR for the GO and MGO show similar bands in the characteristic bonds. However a lower transmittance for the MGO is observed, which is associated to a higher abundance of bonds in the MGO than in the GO. In addition, the bands for the GO are similar to the ones reported in previous works from the literature, such as in Ref. [38]. Also, the importance of the modifications of the synthesis as well as the conditions at which the synthesis is developed are highlighted in Ref. [35].

The ferrihydrite is synthesized using the method proposed in Ref. [39] in which Ferric chloride is used as a precursor. For the first characterization, a FTIR is developed to the synthesized materials. It is observed that in a region between 3000 cm^{-1} and 3500 cm^{-1} the bond ($\text{O}-\text{H}$) is present in a wide band related to the hydroxyl group, which forms part of either the crystalline structure or water retained on the material. In a region between 1300 cm^{-1} and 1650 cm^{-1} it is observed a bond of carbon-oxygen ($\text{C}-\text{O}$) which is produced by the oxidation. The bonds $\text{Fe}-\text{O}$ are shown in the bands between 705 cm^{-1} and 565 cm^{-1} [40].

3.3. FTIR for materials coupled to ferrihydrite

For the GO coupled to ferrihydrite (GOFH), a FTIR analysis is developed to identify the proper bond of the planar structure as well as the bonds in the Fe insertion on the surface. Fig. 3 shows the synthesized materials based on the GO coupled to ferrihydrite and the MGO coupled to ferrihydrite (MGOFH). It is observed that the results are similar for the two materials. Also, a band in a region between 3000 cm^{-1} and 3500 cm^{-1} is observed for both materials, corresponding to an oxygen-hydrogen ($\text{O}-\text{H}$) bond related to the presence of water molecules on the surface.

The band observed at 680 cm^{-1} is related to the stretching vibrations of the $\text{Fe}-\text{O}$ bond generated on the surface of the GO. The small bands at 1100 cm^{-1} are related to the $\text{C}-\text{O}$ bond due to the laminar structure of the GO. The bands observed in the region between 1300 cm^{-1} and 1600 cm^{-1} are related to the stretching of the carbonyl group. By identifying the main bonds of the precursor materials it is possible to determine the insertion places of the ferrihydrite on the graphene oxide.

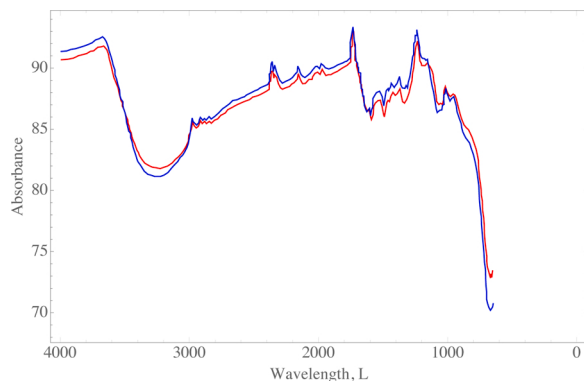


Fig. 3. FTIR for the graphene oxide coupled to ferrihydrite (blue line) and the modified graphene oxide coupled to ferrihydrite (red line).

3.4. FTIR for materials coupled to goethite

Fig. 4 shows the FTIR for the GO coupled to goethite. It is observed a wide band at 3205 cm^{-1} which is related to the stretching vibrations of the oxydril groups (OH). These stretching vibrations are part of either the oxyhydroxide structure of the iron, or the vibrations of the O–H bonds caused by the water molecules adsorbed at the material surface. The bands in the region between 800 cm^{-1} and 950 cm^{-1} are characteristic of the iron hydroxide phase, and correspond to doubling the hydroxile groups Fe–O–OH [41]. A C–OH bond is localized at 1350 cm^{-1} , and is related to the laminar structure of the GO. Also, a C=C bond is found at 1650 cm^{-1} , and is related to the structure of the graphene oxide [35]. By comparing the GOGH and MGOGH materials it is found a similitude in the FTIR analysis. The only difference is the modification made in the synthesis of the GO.

3.5. X-ray characterization

An X-ray characterization (XRD) is developed to analyze the properties of the GO. The precursor for the GO shows a characteristic peak at 26° which corresponds to the (002) plane, denoting its laminar structure. In the case of the GO, the characteristic peak is out of phase to values lower than 2θ , close to 12° . In this case, the values correspond to the plane (001) which shows the laminar structure of graphite, as expected.

Fig. 5 shows the pattern obtained by the X-ray analysis for the GO and MGO materials. A characteristic peaks (001) at 10.71° and 9.36° are observed. These peaks are related to the distance between the layers of the GO and reveal that the oxidation of the graphene is carried out successfully for both syntheses. The peak (001) represents the existence of an intercalated H_2O molecule and an oxygenated functional group

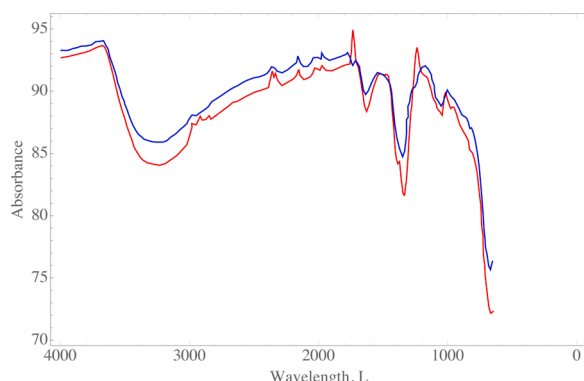


Fig. 4. FTIR for the graphene oxide coupled to goethite (blue line) and the modified graphene oxide coupled to goethite (red line).

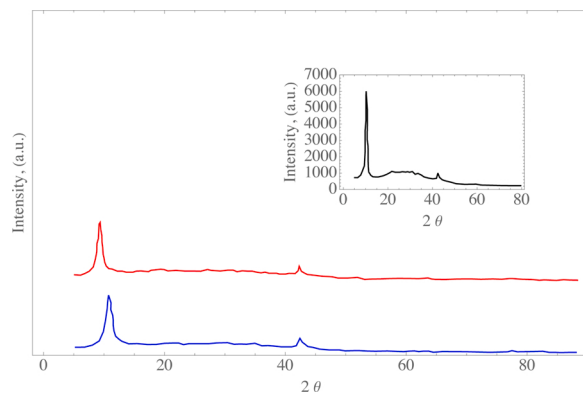


Fig. 5. XRD for the graphene oxide (blue line) and the modified graphene oxide (red line). The insert shows the graphene oxide reported in Ref. [35].

strongly bond to the GO [42]. The variation of the interplanar space for the GO material results from the transition in the oxidation state for the graphite, and is proportional to the oxygen content. **Fig. 5** also shows the X-ray diffraction of the graphene oxide synthesized in Ref. [35] which is similar to the one obtained in the present work.

It is possible to calculate the interplanar distances of the structures in the GO and MGO materials using the data from **Fig. 5** and the Bragg's Law by considering $n = 1$, and $\lambda = 1.54\text{ \AA}$. The results of the interplanar distances for the GO and MGO are shown in **Table 1**. The increase in the interplanar distance for the GO and MGO materials shows the introduction of the oxygenated functional groups in the basal faces of the GO, mainly due to the hydroxide groups and ether. The interplanar distance is bigger for the MGO than for the GO because of the presence of water molecules between layers and to the formation of functional groups that contain oxygen between the layers of the GO.

Fig. 6 shows the X-ray analysis for the GOGH and MGOGH materials. Three peaks are observed in 2θ for each curve. For the MGOGH material, the first peak is located at 10.8° , and can be attributed to the diffraction plane (001) of the GO. The second and third peaks are located at 34.73° and 63.47° , respectively, and can be attributed to the diffraction plane of the goethite iron oxide. For the GOGH material the diffraction peaks attributed to goethite are located at 35.58° and 62.62° ; however, the peak corresponding to the GO looks attenuated when compared with that of the MGOGH, which can be attributed to the position of the crystals.

3.6. Determination of the surface charge distribution

Fig. 7 shows the surface charge distribution for the GOGH and MGOGH materials. The pHZC for the GOGH is of about 7.7 and that for the MGOGH is of about 5.2. Below this value, the surface is charged positively, which represents an ideal feature for the electrostatic attraction of As(V) ions. At those pH values, As(V) is present as $[\text{AsO}_4]^{2-}$ and $[\text{H}_2\text{AsO}_4]$ anions. As demonstrated in a previous study, in order for the As(V) anions to coordinate with arsenic hydroxyl ligands, the surface must allow for the anion's attraction [24]. The charge distribution of the materials comes from the deprotonation and dissociation of terminal and bridge hydroxyl groups of the iron oxyhydroxides. It is interesting to note that these pHZC are considerably

Table 1

Interplanar distance for the graphene oxides and the modified graphene oxides.

Material	Diffraction angle	Crystallographic planes	Interplanar distance (\AA)
GOFH	10.71	(001)	8.287
GOGH	42.45	(100)	2.281
MGOFH	9.36	(001)	9.469
MGOGH	42.30	(100)	2.289

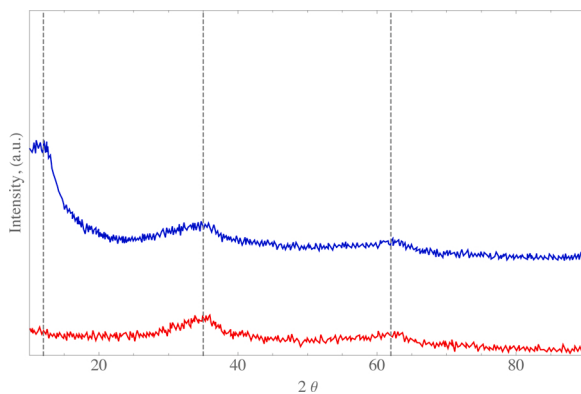


Fig. 6. XRD for the graphene oxide coupled to goethite (blue line) and the modified graphene oxide coupled to goethite (red line).

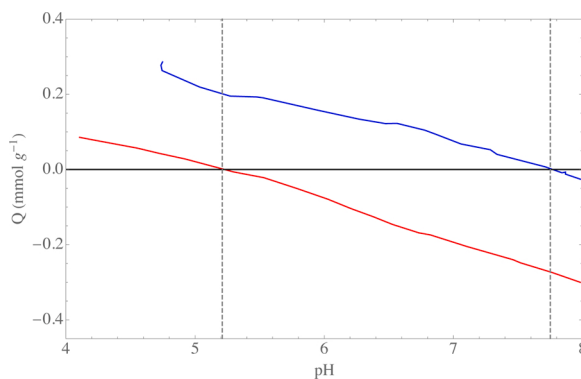


Fig. 7. Surface charge distribution for the graphene oxide coupled to goethite (blue line) and the modified graphene oxide coupled to goethite (red line).

more acidic than those of ferrihydrite and goethite. This suggests that nucleation and condensation of iron complexes over GO result in the exposition of a higher amount of acidic hydroxyl groups of an acidic nature; thus, decreasing the PHPZC.

Based on the results of the characterization, it is suggested that the GO acts as a template for the nucleation of the iron oxyhydroxides. The higher extend of the MGO materials creates a better dispersion of iron hexaaquo complexes. Upon increase in pH, the olation/oxolation reactions allow for the condensation of the oxyhydroxides. Since the GO partially stabilizes the surface during condensation, it helps to decrease the particle size of the iron oxyhydroxides and also to distribute surface groups by not allowing an agglomeration and, therefore, yielding a

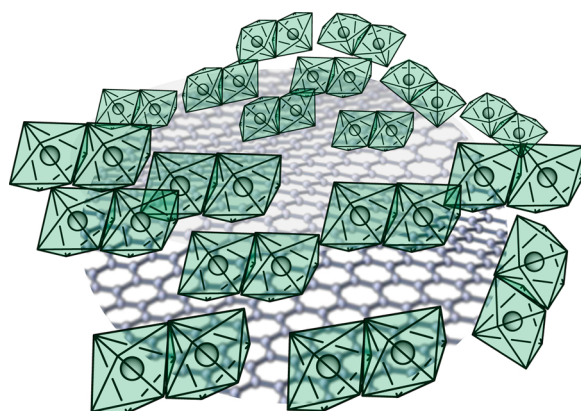


Fig. 8. Conceptualization of iron octahedra nucleation and condensation on the surface of the graphene.

higher amount of hydroxyl groups. A conceptualization of the oxyhydroxides deposition over the GO material is represented in Fig. 8.

3.7. Determination of the specific surface area

The determination of the surface area and pore volume is developed with the technique of nitrogen adsorption. This is a standard technique for the analysis of mesoporous materials. A specific surface area of $4 \text{ m}^2 \text{ g}^{-1}$ is found for the GO. This value is below the values of about $20\text{--}40 \text{ m}^2 \text{ g}^{-1}$ reported in Ref. [43]. Also, it is reported in Ref. [43] that the value of the surface area can vary due to different factors, such as the stiffness and beds of the laminar structure, as well as the dimensions of the samples. These factors cause that the nitrogen molecule is not able to get into the laminar space of the GO. This explains the difference in the values obtained in the present work with respect to those reported in Ref. [43].

The value of the specific surface area for the GOFH synthesized in the present work is $287 \text{ m}^2 \text{ g}^{-1}$. This value is in agreement with the values reported in the literature, i.e., values for the specific surface area of about $200\text{--}500 \text{ m}^2 \text{ g}^{-1}$ are reported in Ref. [40]. On the other hand, the value of the specific surface area for the GOGH synthesized in the present work is $22 \text{ m}^2 \text{ g}^{-1}$. Also, this value is in agreement with the values reported in the literature, i.e., values for the specific surface area of about $21.98\text{--}103 \text{ m}^2 \text{ g}^{-1}$ are reported in Ref. [44]. In addition, the formation and growth of the iron oxide on the surface of the GO depends on the conditions of the synthesis, such as the flow rate at which the ferric solution is added to the graphene oxide suspension and the homogeneous and constant stirring rate [40].

Table 2 shows the values of the characteristic of the specific surface area for the coupled materials. It is observed that all the materials can be considered as mesoporous. Also, the MGOGH shows a smaller specific surface area than the GOGH. However, the pore diameter of the GOGH is bigger than that of the MGOGH and all the coupled materials. In addition, the GOFH shows a bigger specific surface area and pore diameter than the MGOFH.

Fig. 9 shows the pore size distribution (PSD). The calculation is developed by using the BJH method which assumes that pore filling due to condensation represents a well-defined interface in the pores. All the material showed to have a maximum of volume in pores of about 3.5 nm, indicating that most of the pores in the materials are narrow mesopores. This result is in agreement with other studies that have reported average pore diameters between 3 and 4 nm of iron oxides [45]. The highest volume is observed in the MGOGH which also has a shoulder at a pore width of 5 nm. It is also observed that both GO composites have similar surface areas; however, pore variety is larger in the MGO material. It is possible that the highest and more diverse of oxygen groups formed on the MGO are creating a more disperse pore size distribution as a result of the highest nucleation centers. This effect is also present in the ferrihydrite composites in a lower extent. In this material, the peak at 3.5 nm average pore size is shifted to 3.8 nm reinforcing the hypothesis that the MGO expands the iron oxyhydroxide condensations during the synthesis of the material.

The Raman analysis is developed in the range of $1100\text{--}2000 \text{ cm}^{-1}$ and is shown in **Fig. 10**. The typical D and G bands of GO are observed at 1340 cm^{-1} and 1580 cm^{-1} , respectively, and are assigned to the out of plane vibration mode of the sp^2 carbon atoms of defect and E_{2g} photons respectively. Both bands have a similar intensity because the Hummer's

Table 2
Surface area for the graphene oxides and the modified graphene oxides.

Material	Area ($\text{m}^2 \text{ g}^{-1}$)	$V_{\text{pore}} (\text{cm}^3 \text{ g}^{-1})$	$D_{\text{pore}} (\text{nm})$
GOGH	225	0.18	2.83
GOFH	209	0.16	3.19
MGOGH	223	0.18	3.27
MGOFH	183	0.13	2.44

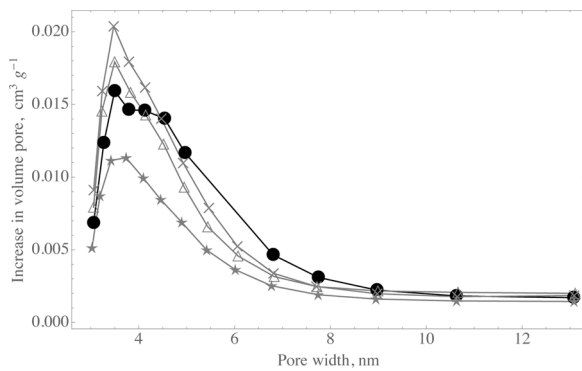


Fig. 9. Pore size distribution for the composite materials obtained with the BJH method. The -x- correspond to GOGH, the -Δ- correspond to GOFH, the -o- correspond to MGOGH, and the -★- correspond to MGOFH.

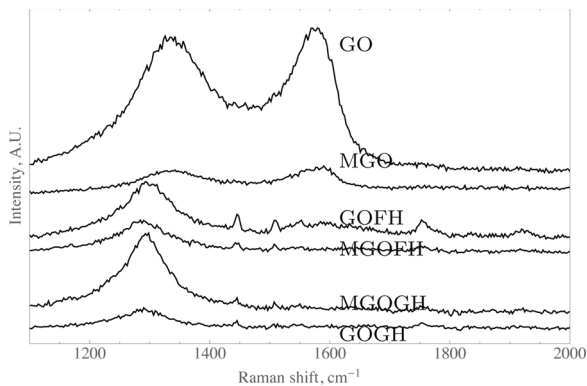


Fig. 10. Raman spectra of the graphene oxide, modified graphene oxide, and composite materials.

strong oxidation induces a strong structural disorder [46]. It is interesting to note that only the D band is present in all the iron oxyhydroxide materials. This confirms the presence of carbon in the composite materials. This band is shifted from 1340 cm^{-1} to lower wavelength values, i.e. 1295 cm^{-1} . This shift also suggests the interaction of π electrons with the iron octahedra and a charge transfer from the graphene oxide sheets [47,48].

The lack of the G band on the composite materials may be related to the laser penetration into the composite materials and to the particular orientation of the ordered carbon on the composites. It could also mean that most of the ordered carbon is lost during the synthesis. In addition, the lack of the D band on the composite materials needs to be studied further.

The XPS of MGOGH demonstrated that the richness of functional groups on the material. The deconvoluted spectra of C1s demonstrated peaks at 289.18 related with O=C-OH (carboxylic), at 288.18 related with C=O, at 287.13 (C-O-C), at 286.28 (C-OH), at 284.88 (adventitious carbon [5]), and 284.08 (C=C). The XPS spectra are similar to that of graphene oxide with a strong degree of oxidation [6]. This result indicates that MGO structure maintains its functionality even after the composite formation (Fig. 11).

3.8. Adsorption characterization

To determine the As(V) adsorption capacity, each coupled material is tested using an adsorption test at 25°C and a pH of 4. The isothermal adsorption tests are compared with the Langmuir and Freundlich models. The regression data are shown in Table 3. The quality of the model is tested with the calculation of the Pearson coefficient as well as the square error, given as

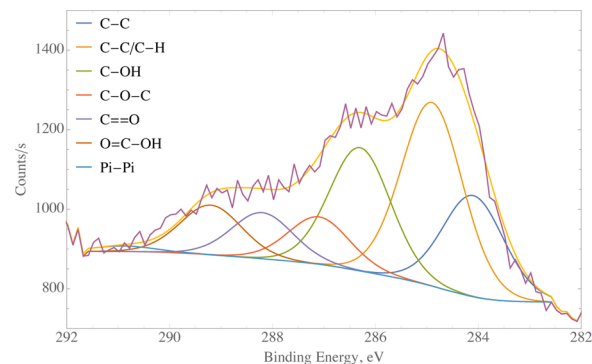


Fig. 11. XPS spectra of the graphene oxide, modified graphene oxide, and composite materials.

Table 3

Adsorption capacities of the coupled materials at a pH of 4 and 25°C .

Material	Langmuir			
	Q	b	R^2	SE
GOFH	18.53	-0.96	0.24	27.56
GOGH	33.63	-1.74	0.31	31.09
MGOFH	40.62	184.7	0.66	8.10
MGOGH	60.41	7.70	0.90	6.14

Material	Freundlich			
	K_F	n	R^2	SE
GOFH	22.19	0.47	0.97	41.46
GOGH	37.81	0.36	0.82	13.49
MGOFH	34.69	0.13	0.85	7.32
MGOGH	44.79	0.23	0.97	4.91

$$\text{SE} = \left(\frac{\sum_{i=1}^N (q_i - q'_i)^2}{N - 2} \right)^{1/2} \quad (8)$$

where q_i represents the mean concentration, and q'_i is the predicted model. The standard error is related to a measure of the relation between the dispersion and the individual observation with respect to the mean value.

It is observed that the R^2 shows values close to 1 and the SE shows relative low values for all the materials, suggesting that the Freundlich and Langmuir models fit reasonable good the experimental data. The results also show that the materials coupled to goethite have a better adsorption capacity than the materials coupled to ferrihydrite. In addition, the value of n for the Freundlich model, which is related to the adsorption intensity, is predicted from the regression analysis. Values of $n < 1$ are related to a physisorption process, which is favorable for a later desorption process.

The results also show that the values of R^2 for the Langmuir model are lower than those of the Freundlich model, and the values of SE are very similar for both models, suggesting that the Freundlich model is the best model to approximate the data.

3.8.1. Isotherms for the MGOGH

The parameters for the As(V) adsorption isotherms at 25°C , 35°C , and 45°C for the selected pH are shown in Table 4. It is observed that the Freundlich model provides a better fitting than the Langmuir model for all the temperatures. A Pearson coefficient bigger than 0.9 for the Freundlich model suggests that this model predicts the phenomena reasonably well. Also, as it is expected, the adsorption capacity increases with temperature because the adsorption phenomena is related to the motion of molecules; that is, the probability of attraction of the

Table 4
Adsorption capacities of the coupled materials at three pH.

Langmuir					
Temperature	pH	Q	b	R ²	SE
25 °C	4	60.4099	7.7031	0.8950	6.1422
	6	52.5349	3.2383	0.9088	5.4377
	8	48.7696	1.7883	0.9108	3.9408
35 °C	4	65.0527	5.8317	0.8989	6.9306
	6	44.4239	1.3508	0.7144	7.5148
	8	47.8213	2.2156	0.9065	4.0437
45 °C	4	66.8868	4.2994	0.9519	5.1227
	6	45.8210	12.1980	0.7549	7.1610
	8	37.0375	0.7826	0.9144	2.9348

Freundlich					
Temperature	pH	K _F	n	R ²	SE
25 °C	4	44.7915	0.2341	0.9659	4.9103
	6	36.0622	0.2178	0.9600	4.1150
	8	27.8574	0.2941	0.9585	3.7406
35 °C	4	47.1792	0.2527	0.9823	3.9106
	6	25.2892	0.2664	0.9007	5.3230
	8	28.7214	0.2808	0.9777	2.7002
45 °C	4	47.3583	0.2339	0.9758	4.4417
	6	34.4845	0.2240	0.9714	3.3749
	8	17.0287	0.3280	0.9862	1.3804

molecules is expected to increase when the molecules are moving faster. The highest value for the adsorption capacity is obtained with a temperature of 45 °C and a pH of 4. It is interesting to note that this value might be related to the superficial charge of the MGOGH with a value of 5.17. This is because the positive surface charge suggest that the material shall attract the arsenite ions with higher intensity and, thus, increase the adsorption capacity.

Fig. 12 shows the curves obtained from the non linear regression of the Freundlich model. It is observed that as the pH is increased, the coupled material has a lower adsorption capacity.

The accuracy of the fitting is evaluated using the standardized residuals defined as the ratio of the residuals over the estimated variance. Fig. 13 shows the standardized residuals for the regression model used in the isotherms. It is observed that the values of the standardized residuals vary from -2 to 2 and are randomly distributed around the x axis. This suggests that the predicted values are close to the measured values with no over or under estimation of the overall prediction. It is also observed that there is no pattern suggesting an error due to the models chosen. Thus, it is assured that the model fits reasonably well the measured values.

Fig. 14 shows the regression obtained with the non-linear van't Hoff equation. It is observed that the constant K_d has a non-linear dependence on $1/T$ for pH of 6 and 8, whereas for a pH of 4 it is close to a linear behavior. The non-linear regressions for pH of 6 and 8 suggest that there are more than one kind of interaction in the adsorption process, and that each of the adsorption mechanisms is affected differently by the temperature. From the regression analysis, it is observed that the entropy change is negative for a pH of 4 ($\Delta S^0 = -109.74 \text{ kJ kmol}^{-1} \text{ K}^{-1}$) and for a pH of 8 ($\Delta S^0 = -60.30 \text{ kJ kmol}^{-1} \text{ K}^{-1}$), whereas the entropy change is positive for a pH of 6 ($\Delta S^0 = 198.04 \text{ kJ kmol}^{-1} \text{ K}^{-1}$). These results imply a decrease of the adsorption sites for pH of 4 and 8, and an increase of the adsorption cites for a pH of 6. Also, the Parson coefficient is lower than 0.7 for a pH of 6. In addition, the enthalpy change implies that the reaction is exothermic for the three pH, i.e., $\Delta H^0 < 0$.

3.8.2. Adsorption kinetics for the MGOGH

The adsorption kinetics is evaluated for pH of 4 and 6, because these pH are related to a higher adsorption capacity for temperatures of 25 °C and 35 °C. The material is tested for 48 h.

In order to evaluate the order of the kinetics for the adsorption process, first and second order models are compared. The models are

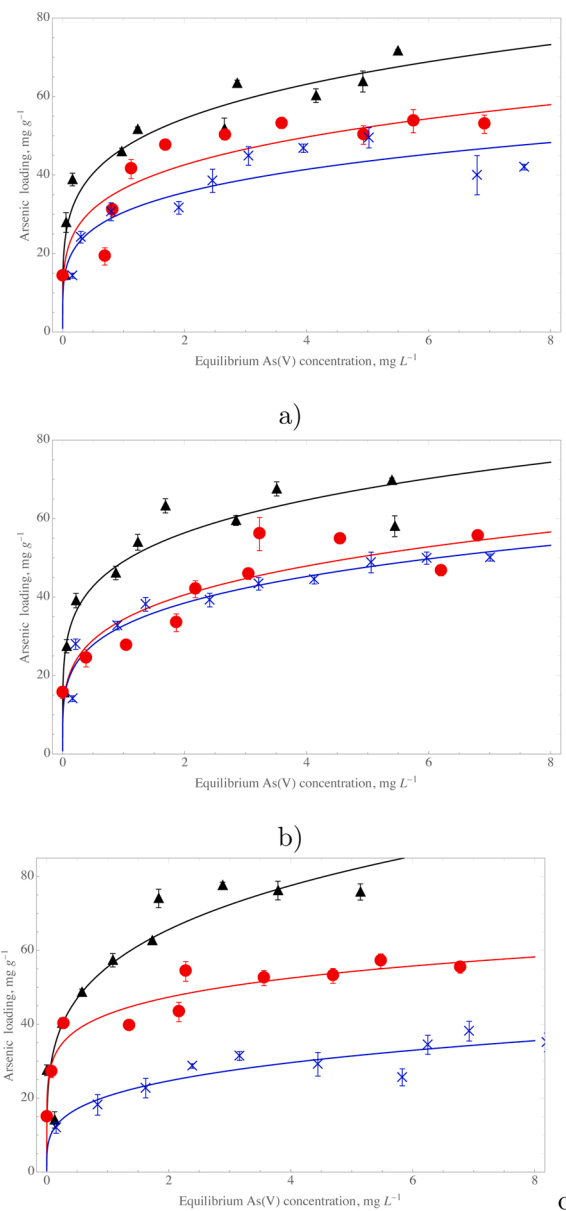


Fig. 12. Isotherms for the coupled materials at (a) 25 °C, (b) 35 °C, and (c) 45 °C. The black, red, and blue lines represent the isotherms at a pH of 4.0, 6.0, and 8.0, respectively. The black -Δ-, the red -○-, and the blue -×- represent the experimental results and their uncertainties (error bars) at a pH of 4.0, 6.0, and 8.0, respectively.

tested using a least square method to determine which is the best fitting model. The Pearson coefficient, R^2 , and the standard error, SE , are calculated for each kinetic model. The kinetic model with the smaller SE is the one that describes better the experimental data.

Table 5 shows the values of the velocity constants for the adsorption, K , and the Pearson coefficients, R^2 , for the MGOGH. It is observed that the Pearson coefficient changes between 0.98 and 0.99, whereas the value of K changes between $0.007 \text{ L mg}^{-1} \text{ min}^{-1}$ and $0.012 \text{ L mg}^{-1} \text{ min}^{-1}$. It is also observed that the value of K increases with temperature. These values are in agreement with the results given by other authors [49].

As can be observed, the first order kinetic model has a slightly higher R^2 value than the first order kinetic model. The accuracy for the two kinetic models is shown in Fig. 15. It is observed that the residuals are distributed randomly around the x axis with a maximum value of 2.3. These results suggest that the regression analysis describes the model

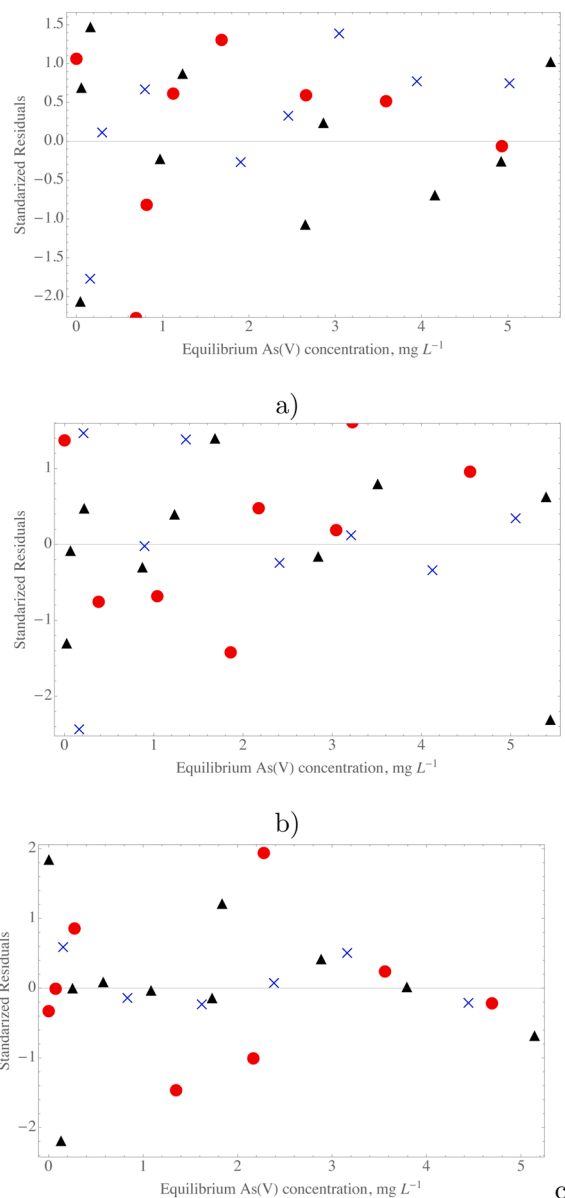


Fig. 13. Standardized residuals for the coupled materials at (a) 25 °C, (b) 35 °C, and (c) 45 °C for a pH of 4.0 (black -△-), 6.0 (red -○-), and 8.0 (blue -×-).

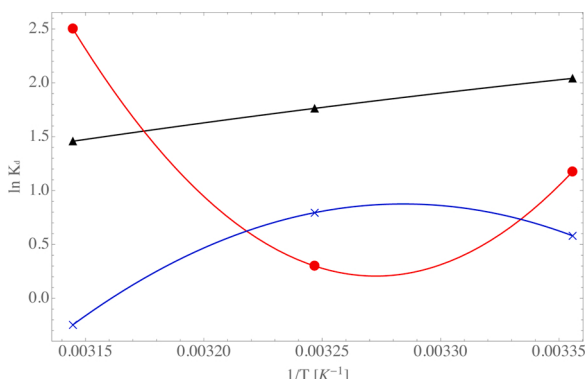


Fig. 14. Non-linear van't Hoff regression for the modified graphene oxide coupled to goethite. The black line with -Δ- corresponds to a pH of 4, the red line with -○- corresponds to a pH of 6, and the blue line with -×- corresponds to a pH of 8.

Table 5

Comparison of the adsorption constants for the kinetic models for the MGOGH.

pH	Temperature (°C)	First order		Second order	
		K	R ²	K	R ²
4	25	0.004	0.985	0.008	0.987
	35	0.008	0.998	0.012	0.990
6	25	0.003	0.981	0.007	0.988
	35	0.006	0.976	0.012	0.992

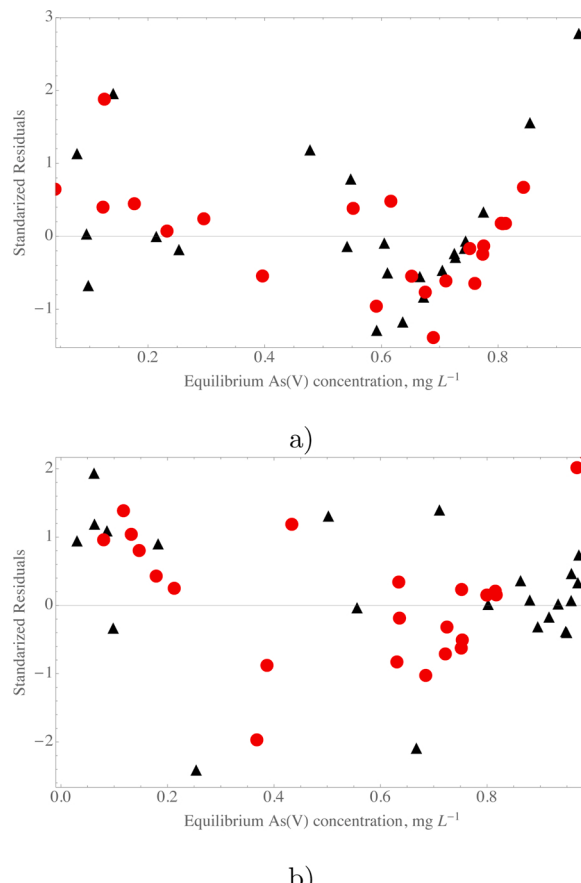


Fig. 15. Standardized residuals for the second order kinetic model at (a) 25 °C and (b) 35 °C. The black -△- correspond to a pH of 4.0 and the red -○- correspond to a pH of 6.0.

reasonable well.

Fig. 16 shows the second order kinetics for the MGO. It is observed that the kinetics at 35° reaches faster the lowest arsenic concentration than the kinetics at 35 °C. These results suggest that the reaction becomes faster as the temperature is increased. Thus, the material is saturated faster at high temperatures than at low temperatures.

3.9. Comparison of the results of the present work with those presented in the technical literature

A direct comparison of adsorption capacities is difficult because the differences between the experimental procedures on the different studies change considerably for the different works reviewed. Thus, the comparison is restricted to the adsorption capacities and the most relevant conditions of each material reviewed from the technical literature.

A comparison of several As adsorbents is shown in Table 6. It is observed that the adsorption capacity of the materials ranges from 0.29 mg g⁻¹ to 124.69 mg g⁻¹. This variability is mostly related, as

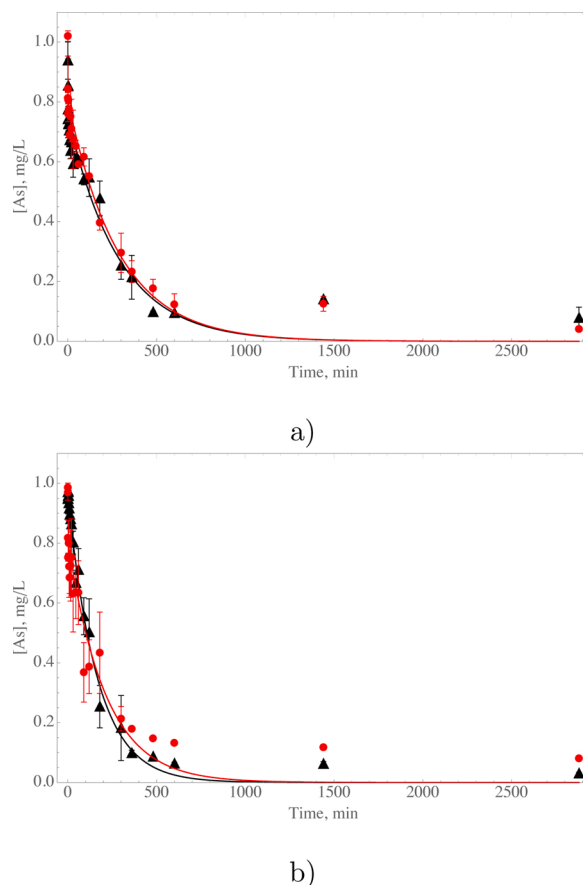


Fig. 16. Adsorption kinetics of the modified graphene oxide at (a) 25 °C and (b) 35 °C. The black - Δ - with uncertainties correspond to a pH of 4.0 and the red - \times - with uncertainties correspond to a pH of 6.0. The solid lines represent a curve fitting of the experimental results.

mentioned above, to the experimental conditions as well as to the synthesis process. It is also observed that the adsorption capacity of the MGOGH material synthesized in the present work is higher than all the proposed material in the literature except those materials with an additional metallic compound like the GO/CuFe₂O₄ proposed in Ref. [50] and the CeO₂/Fe₂O₃/graphene proposed in Ref. [51]. These results suggest that the MGOGH material proposed in the present work has a potential application to remove arsenic in real-life applications.

4. Conclusions

In the present work, the Hummers method and the modified Hummers method are used to synthesize GO with the aim to improve the oxygenated groups (MGO). The synthesized materials are characterized by FTIR, X-ray, adsorption isotherms, and adsorption kinetics. The FTIR results show characteristic bands of the GO reported previously in the technical literature. The X-ray analysis shows an increase in the interplanar distance for the MGO. The increase of the interplanar distance is associated with a higher presence of oxygenated groups in the basal plane.

The GO and MGO materials are also coupled to ferrihydrite and goethite ferric hydroxides in order to improve their adsorptive properties in As(V) solutions. The coupled materials are also characterized by FTIR, X-ray, adsorption isotherms, and adsorption kinetics. The characterization analysis shows that the MGO material coupled to goethite has the highest adsorption capacity which is of about 66 $\mu\text{g g}^{-1}$ at a temperature of 45 °C and a pH of 4. The surface adsorption is compatible with a multilayer adsorption according to the Freundlich model which shows a Pearson coefficient of about 0.98. The characterization by kinetic adsorption shows that the first order rate equation is compatible with the adsorption kinetic for the MGO material at a pH of 4. Also, a second order rate equation is compatible with the adsorption kinetic at a pH of 6. In addition, the kinetic constant increases with temperature and pH, as expected.

The results obtained in the present work suggest that the modification of the Hummers method, together with the coupling of ferric hydroxides, is a useful tool to improve the adsorption properties of As(V).

Author contributions

M. Vazquez-Jaime developed the work and contributed to the development of the paper; Adriana Saldaña-Robles and J. A. Arcibar-Orozco conceived the idea of the research, supervised the development of the project and the characterization of the materials as well as its discussions; Cesar E. Damián-Ascencio, A. L. Saldaña-Robles, M. Martínez-Rosales, and Sergio Cano-Andrade contributed on the thermodynamic model and wrote the paper. All authors have read and agreed to the published version of the manuscript.

Conflict of interest

The authors declare that there is no conflict of interest.

Acknowledgements

This work was partially supported by the Universidad de Guanajuato

Table 6

Comparison of As removal by the materials synthesized in the present work and those reported in the technical literature.

Composites	Adsorption capacity (mg g^{-1})	pH	Isotherm	Concentration (mg L^{-1})	Temperature (°C)	Ref.
MGOGH	66.88	4	Langmuir	1–10	40	Present work
Fe(OH) ₃ -GO	23.78	–	–	51.14	–	[52]
Fe ₃ O ₄ -rGO-MnO ₂	12.22	7	Langmuir	1–10	25.5	[53]
FeOOH GO-COOH	45.70	3–10	Langmuir	1–200	–	[54]
M-GO	38.00	4	Langmuir	–	25	[55]
FeMnO _x /RGO	54.71	7	Langmuir	0.2–7.0	25	[56]
Pirita (Fe ₂ O ₃)	0.29	9	Langmuir	0.01–0.3	25	[57]
FeOOH/ γ -Al ₂ O ₃	4.26	3–10	Langmuir	10–100	25	[58]
Fe-TiOx	40.00	5.5	Langmuir	10–200	50	[59]
GO/CuFe ₂ O ₄	124.69	7.2	Langmuir	5–500	50	[50]
CeO ₂ /Fe ₂ O ₃ /graphene	84.34	3	Langmuir	10–50	–	[51]
Fe3O4-RGO	5.83	7	Langmuir	3–7	20	[60]
Fe3O4-GO	59.60	6.5	Langmuir	–	25	[61]
Fe-GO	3.26	6.5	Langmuir	0.1–5	25	[62]
Fe3O4-RGO	16.00	7	Langmuir	1–10	23	[63]
a-Fe2O3-Fe3O4-GO	26.76	5	Langmuir	1–30	25	[64]

under grant no. DAIP-CIIC 144/2019. A.S.-R. thanks to the Laboratory of Research and Characterization (ICAMM-UG) for its support in the SEM analysis. M.V.-J. is supported by a CONACyT grant. The authors gratefully acknowledge the financial support of the National Council of Science and Technology (CONACyT), Mexico, under its SNI program.

References

- [1] S. Gazzari, D. Cortés-Arriagada, Interaction of trivalent arsenic on different topologies of Fe-doped graphene nanosheets at water environments: a computational study, *J. Mol. Liq.* (2019) 111137.
- [2] W.R. Gallegos-Perez, A.C. Reynosa-Martinez, C. Soto-Ortiz, M.A. Alvarez-Lemus, J. Barroso-Flores, V.G. Montalvo, E. Lopez-Honorato, Effect of UV radiation on the structure of graphene oxide in water and its impact on cytotoxicity and As (III) adsorption, 2019 arXiv preprint arXiv:1905.12167.
- [3] H. Su, Z. Ye, N. Hmidi, High-performance iron oxide-graphene oxide nanocomposite adsorbents for arsenic removal, *Colloids Surf. A: Physicochem. Eng. Asp.* 522 (2017) 161–172.
- [4] A.I.A. Sherlala, A.A.A. Raman, M.M. Bello, A. Buthiyappan, Adsorption of arsenic using chitosan magnetic graphene oxide nanocomposite, *J. Environ. Manag.* 246 (2019) 547–556.
- [5] M.B. Baskan, A. Pala, A statistical experiment design approach for arsenic removal by coagulation process using aluminum sulfate, *Desalination* 254 (1–3) (2010) 42–48.
- [6] S. Bordoloi, S.K. Nath, S. Gogoi, R.K. Dutta, Arsenic and iron removal from groundwater by oxidation-coagulation at optimized pH: laboratory and field studies, *J. Hazard. Mater.* 260 (2013) 618–626.
- [7] A.J. Bora, S. Gogoi, G. Baruah, R.K. Dutta, Utilization of co-existing iron in arsenic removal from groundwater by oxidation-coagulation at optimized pH, *J. Environ. Chem. Eng.* 4 (3) (2016) 2683–2691.
- [8] F.G. Jahromi, A. Ghahreman, In-situ oxidative arsenic precipitation as scorodite during carbon catalyzed enargite leaching process, *J. Hazard. Mater.* 360 (2018) 631–638.
- [9] A. Maghsodi, L. Adlnasab, In-situ chemical deposition as a new method for the preparation of Fe3O4 nanoparticles embedded on anodic aluminum oxide membrane (Fe3O4@AAO): characterization and application for arsenic removal using response surface methodology, *J. Environ. Chem. Eng.* 7 (5) (2019) 103288.
- [10] B. Li, T. Zhang, Z. Yang, Immobilizing unicellular microalgae on pellet-forming filamentous fungus: can this provide new insights into the remediation of arsenic from contaminated water? *Bioresour. Technol.* 284 (2019) 231–239.
- [11] P.S. Ghosal, K.V. Kattil, M.K. Yadav, A.K. Gupta, Adsorptive removal of arsenic by novel iron/olivine composite: insights into preparation and adsorption process by response surface methodology and artificial neural network, *J. Environ. Manag.* 209 (2018) 176–187.
- [12] D. Mohan, C.U. Pittman Jr., Arsenic removal from water/wastewater using adsorbents – a critical review, *J. Hazard. Mater.* 142 (1–2) (2007) 1–53.
- [13] H.-T. Fan, J. Li, M.-M. Guo, X.-L. Fan, D.-S. Zhang, Z.-J. Su, J. Wang, Removal of arsenic from ammoniacal etching waste liquor by 3-(2-aminoethylamino) propyltrimethoxysilane functionalized silica gel sorbent, *Desalin. Water Treat.* 50 (1–3) (2012) 51–58.
- [14] H.-T. Fan, X. Fan, J. Li, M. Guo, D. Zhang, F. Yan, T. Sun, Selective removal of arsenic (V) from aqueous solution using a surface-ion-imprinted amine-functionalized silica gel sorbent, *Ind. Eng. Chem. Res.* 51 (14) (2012) 5216–5223.
- [15] H.-T. Fan, T. Sun, H.-B. Xu, Y.-J. Yang, Q. Tang, Y. Sun, Removal of arsenic (V) from aqueous solutions using 3-[2-(2-aminoethylamino) ethylamino] propyl-trimethoxysilane functionalized silica gel adsorbent, *Desalination* 278 (1–3) (2011) 238–243.
- [16] T.J. Bandosz, J. Jagielo, C. Contescu, J.A. Schwarz, Characterization of the surfaces of activated carbons in terms of their acidity constant distributions, *Carbon* 31 (7) (1993) 1193–1202.
- [17] S. Dixit, J.G. Hering, Comparison of arsenic (V) and arsenic (III) sorption onto iron oxide minerals: implications for arsenic mobility, *Environ. Sci. Technol.* 37 (18) (2003) 4182–4189.
- [18] J.A. Arcibar-Orozco, M. Avalos-Borja, J.R. Rangel-Mendez, Effect of phosphate on the particle size of ferric oxyhydroxides anchored onto activated carbon: As (V) removal from water, *Environ. Sci. Technol.* 46 (17) (2012) 9577–9583.
- [19] S. Luther, N. Borgfeld, J. Kim, J.G. Parsons, Removal of arsenic from aqueous solution: a study of the effects of pH and interfering ions using iron oxide nanomaterials, *Microchem. J.* 101 (2012) 30–36.
- [20] Z. Wei, R. Xing, X. Zhang, S. Liu, H. Yu, P. Li, Facile template-free fabrication of hollow nestlike α -Fe₂O₃ nanostructures for water treatment, *ACS Appl. Mater. Interfaces* 5 (3) (2012) 598–604.
- [21] J.A. Arcibar-Orozco, J.C. Rios-Hurtado, J.R. Rangel-Mendez, Interactions between reactive oxygen groups on nanoporous carbons and iron oxyhydroxide nanoparticles: effect on arsenic (V) removal, *Adsorption* 22 (2) (2016) 181–194.
- [22] S.C.N. Tang, I.M.C. Lo, Magnetic nanoparticles: essential factors for sustainable environmental applications, *Water Res.* 47 (8) (2013) 2613–2632.
- [23] G.K. Das, C.S. Bonifacio, J. De Rojas, K. Liu, K. Van Benthem, I.M. Kennedy, Ultra-long magnetic nanochains for highly efficient arsenic removal from water, *J. Mater. Chem. A* 2 (32) (2014) 12974–12981.
- [24] J.A. Arcibar-Orozco, D.-B. Josue, J.C. Rios-Hurtado, J.R. Rangel-Mendez, Influence of iron content, surface area and charge distribution in the arsenic removal by activated carbons, *Chem. Eng. J.* 249 (2014) 201–209.
- [25] A. Saldaña-Robles, N. Saldaña-Robles, A.L. Saldaña-Robles, C. Damian-Ascencio, V. H. Rangel-Hernández, R. Guerra-Sánchez, Arsenic removal from aqueous solutions and the impact of humic and fulvic acids, *J. Clean. Prod.* 159 (2017) 425–431.
- [26] A. Saldaña-Robles, C.E. Damian-Ascencio, R.J. Guerra-Sánchez, A.L. Saldaña-Robles, N. Saldaña-Robles, A. Gallegos-Muñoz, S. Cano-Andrade, Effects of the presence of organic matter on the removal of arsenic from groundwater, *J. Clean. Prod.* 183 (2018) 720–728.
- [27] K. Krishnamoorthy, M. Veerapandian, K. Yun, S.-J. Kim, The chemical and structural analysis of graphene oxide with different degrees of oxidation, *Carbon* 53 (2013) 38–49.
- [28] A.C. Reynosa-Martínez, G.N. Tovar, W.R. Gallegos, H. Rodríguez-Meléndez, R. Torres-Cadena, G. Mondragón-Solórzano, J. Barroso-Flores, M.A. Alvarez-Lemus, V.G. Montalvo, E. López-Honorato, Effect of the degree of oxidation of graphene oxide on As (III) adsorption, *J. Hazard. Mater.* 384 (2020) 121440.
- [29] S. Thangavel, G. Venugopal, Understanding the adsorption property of graphene-oxide with different degrees of oxidation levels, *Powder Technol.* 257 (2014) 141–148.
- [30] G. Wang, X. Sun, C. Liu, J. Lian, Tailoring oxidation degrees of graphene oxide by simple chemical reactions, *Appl. Phys. Lett.* 99 (5) (2011) 053114.
- [31] D. Cortés-Arriagada, A. Toro-Labbé, Improving As (III) adsorption on graphene based surfaces: impact of chemical doping, *Phys. Chem. Chem. Phys.* 17 (18) (2015) 12056–12064.
- [32] C. Zolezzi, C.F. Ihle, C. Angulo, P. Palma, H. Palza, Effect of the oxidation degree of graphene oxides on their adsorption, flocculation, and antibacterial behavior, *Ind. Eng. Chem. Res.* 57 (46) (2018) 15722–15730.
- [33] W.S. Hummers Jr., R.E. Offeman, Preparation of graphitic oxide, *J. Am. Chem. Soc.* 80 (6) (1958) 1339.
- [34] J.A. Arcibar-Orozco, R. Wallace, J.K. Mitchell, T.J. Bandosz, Role of surface chemistry and morphology in the reactive adsorption of H₂S on iron (hydr) oxide/graphite oxide composites, *Langmuir* 31 (9) (2015) 2730–2742.
- [35] J. Guerrero-Contreras, F. Caballero-Briones, Graphene oxide powders with different oxidation degree, prepared by synthesis variations of the Hummers method, *Mater. Chem. Phys.* 153 (2015) 209–220.
- [36] V. Lenoble, V. Deluchat, B. Serpaud, J.-C. Bollinger, Arsenite oxidation and arsenate determination by the molybdate blue method, *Talanta* 61 (3) (2003) 267–276.
- [37] Y. Liu, Is the free energy change of adsorption correctly calculated? *J. Chem. Eng. Data* 54 (7) (2009) 1981–1985.
- [38] X. Liu, R. Ma, X. Wang, Y. Ma, Y. Yang, L. Zhuang, S. Zhang, R. Jehan, J. Chen, X. Wang, Graphene oxide-based materials for efficient removal of heavy metal ions from aqueous solution: a review, *Environ. Pollut.* (2019).
- [39] U. Schwertmann, R.M. Cornell, Goethite, Iron Oxides in the Laboratory: Preparation and Characterization, 2nd ed., Wiley VCH Verlag, Weinheim, Germany, 2007, pp. 67–92.
- [40] M. Villacís-García, M. Ugalde-Arzate, K. Vaca-Escobar, M. Villalobos, R. Zanella, N. Martínez-Villegas, Laboratory synthesis of goethite and ferrihydrite of controlled particle sizes, *Bol. Soc. Geol. Mex.* 67 (3) (2015) 433–446.
- [41] R.M. Cornell, U. Schwertmann, The Iron Oxides: Structure, Properties, Reactions, Occurrences and Uses, John Wiley & Sons, 2003.
- [42] S. Drewniak, R. Muzyka, A. Stolarczyk, T. Pustelnik, M. Kotyczka-Morańska, M. Setkiewicz, Studies of reduced graphene oxide and graphite oxide in the aspect of their possible application in gas sensors, *Sensors* 16 (1) (2016) 103.
- [43] T. Szabó, V. Hornok, R.A. Schoonheydt, I. Dékány, Hybrid langmuir-blodgett monolayers of graphite oxide nanosheets, *Carbon* 48 (5) (2010) 1676–1680.
- [44] P. Lakshmipathiraj, B.R.V. Narasimhan, S. Prabhakar, G.B. Raju, Adsorption of arsenate on synthetic goethite from aqueous solutions, *J. Hazard. Mater.* 136 (2) (2006) 281–287.
- [45] A. Bumajdad, S. Ali, A. Mathew, Characterization of iron hydroxide/oxide nanoparticles prepared in microemulsions stabilized with cationic/non-ionic surfactant mixtures, *J. Colloid Interface Sci.* 355 (2) (2011) 282–292.
- [46] S.M. Hafiz, R. Ritkos, T.J. Whitcher, N.M. Razib, D.C.S. Bien, N. Chanlek, H. Nakajima, T. Saisopa, P. Songsiririthigul, N.M. Huang, S.A. Rahmana, A practical carbon dioxide gas sensor using room-temperature hydrogen plasma reduced graphene oxide, *Sens. Actuators B: Chem.* 193 (2014) 692–700.
- [47] S. Wang, B.M. Goh, K.K. Manga, Q. Bao, P. Yang, K.P. Loh, Graphene as atomic template and structural scaffold in the synthesis of graphene-organic hybrid wire with photovoltaic properties, *ACS Nano* 4 (10) (2010) 6180–6186.
- [48] Q. Su, S. Pang, V. Aljani, C. Li, X. Feng, K. Müllen, Composites of graphene with large aromatic molecules, *Adv. Mater.* 21 (31) (2009) 3191–3195.
- [49] S.I. Siddiqui, S.A. Chaudhry, Iron oxide and its modified forms as an adsorbent for arsenic removal: a comprehensive recent advancement, *Process Saf. Environ. Prot.* 111 (2017) 592–626.
- [50] L.-K. Wu, H. Wu, H.-B. Zhang, H.-Z. Cao, G.-Y. Hou, Y.-P. Tang, G.-Q. Zheng, Graphene oxide/Cu₂O₄ foam as an efficient adsorbent for arsenic removal from water, *Chem. Eng. J.* 334 (2018) 1808–1819.
- [51] U.K. Sahu, S.S. Mahapatra, R.K. Patel, Application of Box-Behnken design in response surface methodology for adsorptive removal of arsenic from aqueous solution using Ce₂O₃/Fe₂O₃/graphene nanocomposite, *Mater. Chem. Phys.* 207 (2018) 233–242.
- [52] K. Zhang, V. Dwivedi, C. Chi, J. Wu, Graphene oxide/ferric hydroxide composites for efficient arsenate removal from drinking water, *J. Hazard. Mater.* 182 (1–3) (2010) 162–168.
- [53] X. Luo, C. Wang, S. Luo, R. Dong, X. Tu, G. Zeng, Adsorption of As (III) and As (V) from water using magnetite Fe₃O₄-reduced graphite oxide-MnO₂ nanocomposites, *Chem. Eng. J.* 187 (2012) 45–52.

- [54] M.-L. Chen, Y. Sun, C.-B. Huo, C. Liu, J.-H. Wang, Akaganeite decorated graphene oxide composite for arsenic adsorption/removal and its proconcentration at ultra-trace level, *Chemosphere* 130 (2015) 52–58.
- [55] Y. Yoon, W.K. Park, T.-M. Hwang, D.H. Yoon, W.S. Yang, J.-W. Kang, Comparative evaluation of magnetite-graphene oxide and magnetite-reduced graphene oxide composite for As (III) and As (V) removal, *J. Hazard. Mater.* 304 (2016) 196–204.
- [56] Z. Lou, Z. Cao, J. Xu, X. Zhou, J. Zhu, X. Liu, S.A. Baig, J. Zhou, X. Xu, Enhanced removal of As (III)/(V) from water by simultaneously supported and stabilized Fe-Mn binary oxide nanohybrids, *Chem. Eng. J.* 322 (2017) 710–721.
- [57] T. Turk, Removal of dissolved arsenic by pyrite ash waste, *Mine Water Environ.* 36 (2) (2017) 255–263.
- [58] Z. Wang, X. Shen, M. Jing, C. Li, Enhanced arsenic removal from drinking water by FeOOH/ γ -Al₂O₃ granules, *J. Alloys Compd.* 735 (2018) 1620–1628.
- [59] G. García-Rosales, L.C. Longoria-Gándara, G.J. Cruz-Cruz, M.G. Olayo-González, R. Mejía-Cuero, P.Á. Pérez, Fe-TiOx nanoparticles on pineapple peel: synthesis, characterization and As (V) sorption, *Environ. Nanotechnol. Monit. Manag.* 9 (2018) 112–121.
- [60] V. Chandra, J. Park, Y. Chun, J.W. Lee, I.-C. Hwang, K.S. Kim, Water-dispersible magnetite-reduced graphene oxide composites for arsenic removal, *ACS Nano* 4 (7) (2010) 3979–3986.
- [61] G. Sheng, Y. Li, X. Yang, X. Ren, S. Yang, J. Hu, X. Wang, Efficient removal of arsenate by versatile magnetic graphene oxide composites, *RSC Adv.* 2 (32) (2012) 12400–12407.
- [62] G. Gollavelli, C.-C. Chang, Y.-C. Ling, Facile synthesis of smart magnetic graphene for safe drinking water: heavy metal removal and disinfection control, *ACS Sustain. Chem. Eng.* 1 (5) (2013) 462–472.
- [63] B. Paul, V. Parashar, A. Mishra, Graphene in the Fe₃O₄ nano-composite switching the negative influence of humic acid coating into an enhancing effect in the removal of arsenic from water, *Environ. Sci.: Water Res. Technol.* 1 (1) (2015) 77–83.
- [64] F. Yu, S. Sun, J. Ma, S. Han, Enhanced removal performance of arsenate and arsenite by magnetic graphene oxide with high iron oxide loading, *Phys. Chem. Chem. Phys.* 17 (6) (2015) 4388–4397.